Optimal Architecture of a Dual S-Scheme ZnIn$_2$S$_4$−ZnO−Al$_2$O$_3$ Heterosystem with High H$_2$ Evolution Rate under Visible Light

Irshad Ahmad, Shazia Shukrullah,* Humaira Hussain, Muhammad Yasin Naz, Muhammad Irfan, Othman Alyahyawy, and Morooj A. Al thagafi

Read Online

ACCESS | Metrics & More | Article Recommendations

ABSTRACT: In this study, dual S-scheme ZnIn$_2$S$_4$−Al$_2$O$_3$−ZnO (ZIS−Al−Zn) heterojunctions were produced by a facile, low cost, and rapid combustion technique. These heterojunctions accelerated the photocatalytic hydrogen production due to the multi-channel-promoted separation of photocarriers. By optimizing the content of the components, the synthesized ZIS−Al−Zn composite with 20 wt% of ZnIn$_2$S$_4$ and 30 wt% of Al$_2$O$_3$ in the ZIS−Al−Zn composite demonstrated the highest hydrogen production rate of 54.2 mmol g^{-1} h^{-1}, which was nearly 11 and 8.30 times better than ZnO−Al$_2$O$_3$ and ZnO−ZnIn$_2$S$_4$ composites, respectively. The results of DRS, PL, EIS, LSV, and CV techniques showed the highest shift in the light absorption, rapid interfacial transfer, and quenched recombination of photocarriers over the ternary ZIS−Al−Zn composite than single and binary catalysts. The obtained results revealed the formation of a dual S-scheme mechanism of transfer of photocarriers in ZIS−Al−Zn heterojunctions, contributing to better hydrogen production efficiency. The optimized ZIS−Al−Zn composite also exhibited good stability and reusability.
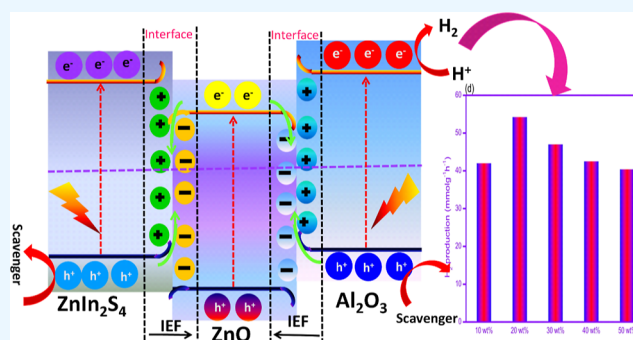
1. INTRODUCTION

The photocatalytic (PC) performance of a unitary candidate, such as pure ZnO, is not upto the mark due to rapid recombination rate of photocarriers (e$^-$/h$^+$), restricted optical absorption, inadequate adsorption capacity, and unsatisfactory stability.[1−3] To avoid these drawbacks, a promising strategy is to design multi-component heterogeneous photocatalysts, where the migration and separation of photocarriers, kinetics, and surface redox potentials are highly increased.[1] Moreover, constructing a promising heterojunction photocatalyst relies on two factors: appropriate band staggered positions of the constituent materials and perfect interfaces for the separation and migration of photocarriers.[2] ZnO is an appealing n-type semiconductor with hexagonal wurtzite composition, which has appeared as decent research material for diverse PC applications due to the following motives: (i) low cost, (ii) eco-friendly, and (iii) appropriate band gap (3.37 eV) with favorable negative conduction band potential (E_{CB} = −0.29 eV vs NHE) to accelerate the PC reaction.[3] The design of ZnO-derived heterojunctions has been established as quite beneficial for scaling up the PC efficiency of ZnO-derived heterojunction photocatalysts.[4] Still, to date, several ZnO-derived hetero-structures with relatively staggered band positions have been researched as outstanding photocatalysts, including ZnO/TiO$_2$,[5] ZnO/g-C$_3$N$_4$,[6] ZnO/CdS,[7] ZnO/WO$_3$,[8] etc.

Aluminum oxide (Al$_2$O$_3$), a natural origin n-type semi-conductor, has emerged as an effective PC technology-support material due to low cost, negligible photochemical reactivity, easy fabrication, impressive thermal stability, non-toxicity, and substantial surface features.[9] When used as an individual catalyst, the Al$_2$O$_3$ activates under UV light due to its large energy band gap. Surprisingly, the band potentials of Al$_2$O$_3$ are (E_{CB} = −0.86, E_{VB} = 2.53 eV vs NHE), which makes it an ideal supporting material to design a heterojunction system for PC H$_2$ evolution.[10] For instance, Janani et al. documented advanced PC activity with strong stability of the CdO$_2$−Al$_2$O$_3$ heterojunction system contrasted to pure CdO catalyst.[11] Several other authors also designed Al$_2$O$_3$-derived heterojunction systems with promising PC performances, such as MnO$_2$−Al$_2$O$_3$,[12] TiO$_2$−Al$_2$O$_3$,[13] Al$_2$O$_3$−CdO,[14] and CeO$_2$−Al$_2$O$_3$.[15] Nevertheless, analogous to unitary photocatalysts, the surface redox reactions efficiency for binary heterosystems is too sluggish, which consequently results in the assembly of

photoelectrons in the CB of one catalyst to enhance the probability of recombination with its VB holes.[16]

Freshly, trifunctional photocatalysts based on a single nano-assembly architecture with different interfaces are fascinating owing to their efficient ability to manifest strong separation and transfer of photocarriers, broadening the optical absorption and enhanced redox ability.[17] For instance, Ma et al.[18] designed a ternary $In_2S_3/CdIn_2S_4/In_2O_3$ heterosystem, which ultimately exhibited 26.7 times improved PC H_2 production performance contrasted to In_2S_3 due to the design of multi-interfaces for the swift transfer and separation of photocarriers (e^-/h^+).[18] Liu et al.[19] reported successfully constructing the type II heterostructure of $GCN-Al_2O_3-ZnO$. They manifested that the designed heterojunction increased separation of photocarriers compared to pure ZnO. However, the swift recombination of photocarriers and relatively more positive conduction band potential (E_{CB}) contrasted to the standard reduction potential of H^+/H_2 (-0.41 eV vs NHE) effectively disturbed the PC activity of Al_2O_3-ZnO.[20] Contrasted to the conventional heterojunctions, a novel S-scheme heterojunction system based on ZnO that served as trifunctional photocatalysts for H_2 production is scarcely researched.[3] The design of a dual S-scheme system consisting of three components can elucidate why photocarriers (e^-/h^+) of powerful redox potentials are preserved, whereas photo-carriers with relatively weaker redox potentials perished.[21] Due to the alignment of different Fermi levels of three components with different work functions, the built-in electric field originates at the interface, which consequently provides band bending and accelerates the transfer of photocarriers.[22]

Consequently, it is important to explore a suitable semiconductor to integrate with Al_2O_3/ZnO to construct an efficient S-scheme trifunctional catalyst with comparatively high contact interfaces. The $ZnIn_2S_4$, an n-type semiconductor has been verified to be a potential candidate owing to its narrow band gap (2.40 eV), non-toxicity, and low cost.[23] With E_{CB} (-0.86 eV vs NHE) and E_{VB} (1.54 eV vs NHE) potentials smaller contrasted to that of ZnO and Al_2O_3, the $ZnIn_2S_4$ can be introduced to design ternary S-scheme heterojunctions with aligned CB and VB edges to produce built-in electric field (IEF) at the interfaces which consequently could control the directional flow of charge carriers.[24] Based on the energy band positions of three semiconductors, the photoelectrons in the CB of ZnO could be transferred to the VB of $ZnIn_2S_4$ and Al_2O_3 through the S-scheme charge transfer mechanism, while photocarriers with strong redox potentials could be retained. Such a heterosystem could efficiently increase the separation of photocarriers and speedup the process of S-scheme charge transmission.

Based on the above reflections, the $ZnIn_2S_4-ZnO-Al_2O_3$ nanoparticles were synthesized via a facile and inexpensive combustion process. The PC activity of the fabricated heterosystem was tested for H_2 production. The following benefits effectively reflect the novelty of the present work: (i) rapid and inexpensive synthesis, (ii) 0D nanoparticles with large surface area and large number of active sites, and (iii) effective photocarriers transfer capability, which ultimately increase the PC performance. Among three semiconductors, $ZnIn_2S_4$ and Al_2O_3 served as reduction catalysts, while ZnO acted as an oxidation photocatalyst. The integration of three semiconductors exhibited a redshift in the optical absorption and strongly enhanced the production of photocarriers (e^-/h^+) owing to the design of dual S-scheme heterojunction. Because

of the energy band alignment of the $ZnIn_2S_4-ZnO-Al_2O_3$ composite, the availability of abundant charge transfer channels through the design of dual S-scheme heterojunction strongly accelerated the transfer and separation of photo-carriers. To our knowledge, the $ZnIn_2S_4-ZnO-Al_2O_3$ dual S-scheme heterojunction system has never been documented previously. Several characterization techniques confirmed that the $ZnIn_2S_4-ZnO-Al_2O_3$ nanoparticles demonstrated promising PC performances for wastewater treatment, H_2 evolution, and strong stability.

2. EXPERIMENTAL PROCEDURES

2.1. Reagents. Zinc nitrate hexahydrate $Zn(NO_3)_2 \cdot 5H_2O$, indium nitrate pentahydrate $In(NO_3)_3 \cdot 5H_2O$, and thiourea $SC(NH_2)_2$ and glycine $C_2H_5NO_2$ were purchased from Sigma-Aldrich and used without any further purification treatments. Deionized water (DIW) was utilized during all experiments.

2.2. Synthesis of Catalysts. $ZnIn_2S_4-ZnO-Al_2O_3$ nanoparticles were fabricated by the solution combustion route. The stoichiometric amounts of the $ZnIn_2S_4$ precursors $[Zn(NO_3)_2 \cdot 5H_2O, In(NO_3)_3 \cdot 5H_2O$ and $SC(NH_2)_2]$ were dissolved in 50 mL of DIW water under constant stirring (1000 rpm) to obtain the solution-A. Similarly, $Zn(NO_3)_3 \cdot 6H_2O$ and $Al(NO_3)_3$ precursors of ZnO and Al_2O_3 with required stoichiometric amounts were dissolved separately to acquire solution-B and solution-C, respectively. Afterward, these three as-prepared solutions were mixed uniformly under constant magnetic stirring to achieve the solution of oxidants (fuel/oxidant = 1.7). Next, the required amount of fuel $(C_2H_5NO_2)$ was added to the oxidants solution under stirring, followed by shifting of the mixture on the pre-heated (75 °C) magnetic stirrer, which was further stirred for 90 min to obtain the homogeneity. Subsequently, the solution temperature was raised to 300 °C under stirring, and meanwhile, the solution was gradually transformed into gel due to the evaporation of water. This gel was then ignited with the liberation of the huge amount of gases because of the combustion process between oxidants and fuel to produce blackish nanopowders, which were subsequently collected and grounded before heating in a furnace at 700 °C for 3 h. Finally, the obtained nanocrystalline powder in white color was named $ZnIn_2S_4-ZnO-Al_2O_3$ (ZIS−Zn−Al) composite nanoparticles. For comparison, $ZnO-ZnIn_2S_4$ (Zn−ZIS), $ZnO-Al_2O_3$ (Zn−Al), $ZnIn_2S_4$, Al_2O_3, and ZnO samples were also prepared using the same combustion process using their respective precursors as oxidants and glycine as fuel under identical experimental conditions.

2.3. Characterization. The structures and phases of the fabricated photocatalysts were analyzed using an X-ray diffractometer (Shimadzu XRD-6000, 2θ: 20−70°, step width: 0.02°, scan rate: 0.05°/min, V: 40 kV, $\lambda_{CuK\alpha}$: 0.15406 nm, I: 40 mA). Surface morphology and elemental analysis were conducted using scanning electron microscopy (SEM) equipment (NovaNano 450, V: 25 kV). Fourier transform infrared (FTIR) (KBr method, 400−4000 cm^{-1}) was performed to determine the functional groups. The N_2 isotherm was used to measure the BET surface area of the photocatalysts. The charge recombination process is understood by recording the room-temperature photoluminescence spectra using a Shimadzu RF-6000 spectrophotometer. The light absorption characteristics and band gap energies were analyzed using diffuse-reflectance spectroscopy (DRS, Shimadzu UV-2450, λ range: 200−800 nm). The photoelectrochem-
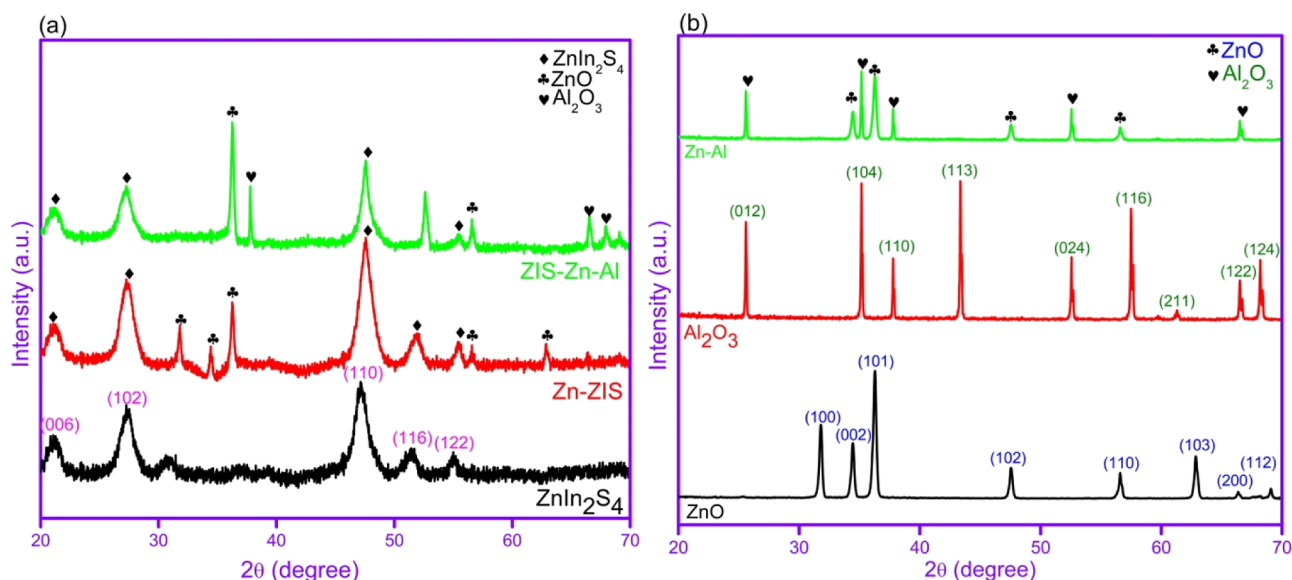
Figure 1. XRD patterns of (a) $ZnIn_2S_4$, Zn−ZIS, and ZIS−Zn−Al; (b) ZnO, Al_2O_3, and Zn−Al catalysts.

ical measurements were performed at room temperature by applying a standard three-electrode workstation CHI660E fitted with a 300 W Xe in a 0.5 M Na_2SO_4 electrolyte solution. A Pt wire (0.6 cm × 8.0 cm) was taken as a counter electrode, while Ag/AgCl was taken as a reference electrode. The catalyst/FTO was applied as the working electrode in these measurements. The working electrode was built using the results of our earlier research.[25] The current response of the prepared catalysts was recorded beneath the above-mentioned Xe lamp for a period of 600 s by switching on and off the light at regular intervals. The MS measurements of the catalysts were recorded from −1 to +1 V at 3 kHz under the dark. The CV tests were conducted by sweeping the voltage from −1 to +1 V with a scan rate of 50 mV/s.

2.4. PC Activity. PC production of hydrogen (H_2) via water-splitting for all the synthesized catalysts was tested in a Pyrex glass reactor. Typically, 30 mL of the aqueous glycerol solution (10 vol %) was utilized as a sacrificial reagent by inserting 10 mg of as-prepared samples under ultrasonication to speed up the water-splitting reaction. Subsequently, the aqueous suspension containing the catalyst was magnetically stirred for 1 h to prevent the agglomeration of catalyst particles. Meanwhile, to get rid of the dissolved molecular gases, the prepared suspension was thoroughly evacuated before the start of the H_2 production reaction. A 300 W Xe lamp, fitted with a UV filter ($\lambda > 400$ nm), was placed at 15 cm from the photocatalysis setup. The PC H_2 production was analyzed with a gas analyzer. For reusability experiments, the PC H_2 reaction was repeated five times using the optimum catalyst and the illumination period of visible light for each run was set as 4 h.

3. RESULTS AND DISCUSSION

3.1. Structural Analysis. The phase structure of the fabricated catalysts was examined via XRD patterns, and the results in Figure 1a,b verified that pure ZnO, Al_2O_3, and $ZnIn_2S_4$ catalysts revealed highly crystalline structures. The XRD patterns of pure ZnO catalyst expressed eight distinct diffraction peaks observed at 31.81, 34.35, 36.28, 47.58, 56.59, 62.82, 66.34, and 69.21°, which were indexed well to the

diffraction planes (100), (002), (101), (102), (110), (103), (200), and (112) of hexagonal wurtzite ZnO (JCPDS # 36-1451), respectively.[6] The absence of stray peaks in the XRD patterns of the ZnO catalyst confirmed the phase purity of as-fabricated ZnO. It can also be observed that diffraction peaks appeared at 21.15, 27.43, 47.15, 52.45, and 55.15° could be satisfyingly indexed to (006), (102), (110), (116), and (022) crystalline planes of $ZnIn_2S_4$, respectively, entirely authenticating the fabrication of a highly crystalline hexagonal $ZnIn_2S_4$ catalyst (JCPDS # 65-2023).[23] The pure Al_2O_3 catalyst showed obvious diffraction peaks at 25.51, 35.22, 37.75, 43.38, 52.52, 57.51, 61.4, 66.54, and 68.15°, which were attributed to (012), (104), (110), (113), (024), (116), (122), (124), and (030) crystal planes of Al_2O_3, respectively (JCPDS # 10-173).[12] After introducing Al_2O_3, the diffraction patterns of the Zn−Al catalyst authenticate the coexistence of ZnO and Al_2O_3 phases, retaining the identical original crystal structures as manifested by the individual materials, implying the successful formation of the Zn−Al composite. In addition, the intensities of diffraction peaks of ZnO and Al_2O_3 were decreased compared to that of individual catalysts, which affirmed that ZnO and Al_2O_3 were integrated into each other.[21] Significantly, the XRD patterns of the Zn−ZIS catalyst exhibited the diffraction peaks of both ZnO and $ZnIn_2S_4$, implying that $ZnIn_2S_4$ had been successfully coupled with ZnO. As for the ZIS−Zn−Al catalyst, it was easy to observe that the diffraction signal of ZnO, Al_2O_3, and $ZnIn_2S_4$ appear simultaneously in the XRD patterns of ZIS−Zn−Al catalyst, which strongly claim the triumphant integration of ZnO, Al_2O_3 and $ZnIn_2S_4$ in ZIS−Zn−Al composite. It is noteworthy that the main diffraction peaks of the ZIS−Zn−Al catalyst manifested a slight shift toward smaller 2θ when Al_2O_3 and $ZnIn_2S_4$ are integrated with ZnO, which might be explained on the basis of successful integration among ZnO, Al_2O_3, and $ZnIn_2S_4$.

3.2. SEM and EDX Analysis. The surface morphology of the prepared ZnO, Al_2O_3, $ZnIn_2S_4$, and ZIS−Zn−Al catalysts was examined by SEM analysis. Figure 2a,b shows that nanoparticles of individual components ZnO and Al_2O_3 proned to aggregate into non-uniform particles, which occupy the small surface area and ultimately reduce the PC activity. The $ZnIn_2S_4$ in Figure 2c manifested a large number of
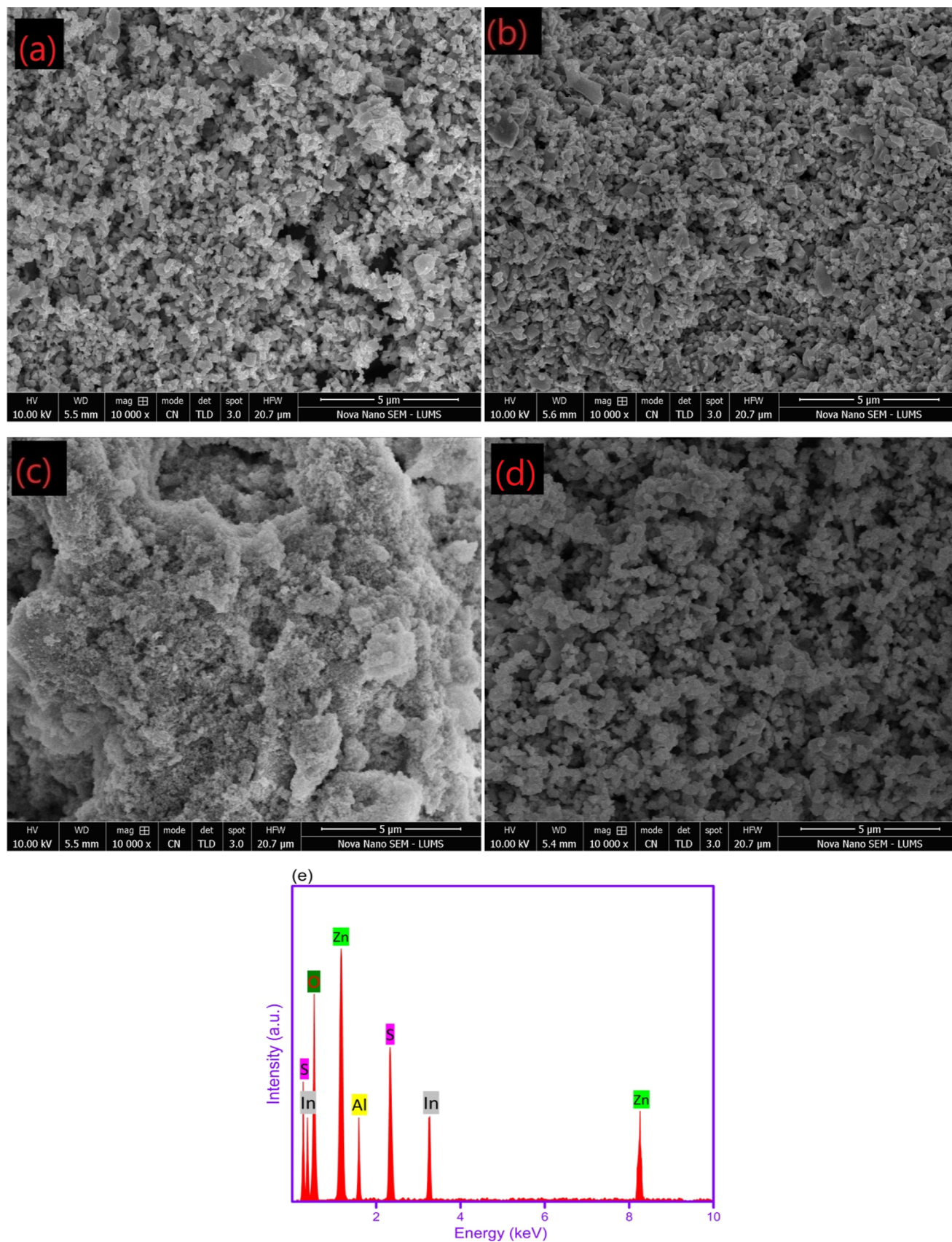
Figure 2. SEM micrographs of (a) ZnO; (b) Al_2O_3; (c) $ZnIn_2S_4$; and (d) ZIS−Zn−Al catalysts and (e) EDX spectra of the ZIS−Zn−Al catalyst.

irregular and agglomerated nanoparticles with porous surfaces. In contrast, the ZIS−Zn−Al catalyst (Figure 2d) showed relatively uniform and smaller particles, which promote surface area and number of active sites for PC H_2 production.
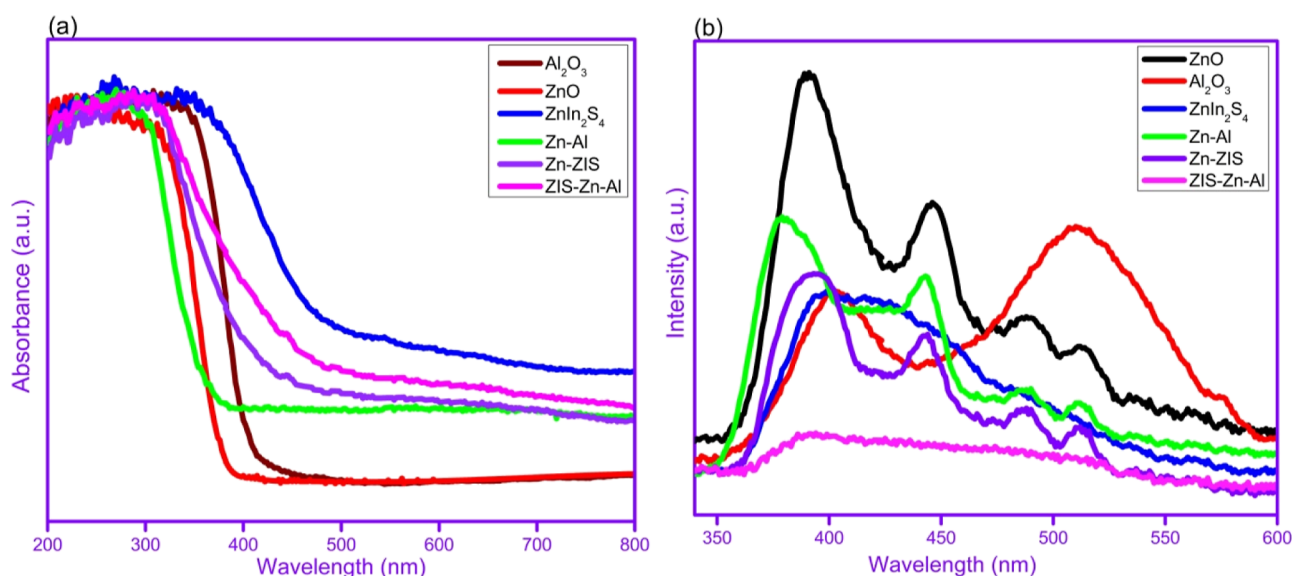
Figure 3. (a) UV−vis spectra and (b) PL analysis of as-prepared catalysts.

Meanwhile, 0D nanoparticles could abbreviate the transport of photoelectrons to reach the surface, avoiding their bulk recombination to trigger the surface catalytic reaction. Figure 2e shows that the EDX analysis confirmed the presence of S, In, O, Zn, and Al elements in the EDX spectra of the ZIS−Zn−Al catalyst, confirming the co-existence of $ZnIn_2S_4$, ZnO, and Al_2O_3 materials.

3.3. Optical Absorption Analysis. Strong optical absorption characteristics of the material identify its more charge carrier's formation ability.[15] As shown in Figure 3a, ZnO demonstrated an absorption edge at 383.6 nm, corresponding to the optical band gap of 3.23 eV. In contrast, the absorption edge of the Al_2O_3 catalyst pronged to 396 nm, revealing that the optical band gap is 3.14 eV. This indicates that ZnO and Al_2O_3 demonstrated light absorption ability only in the UV region, identifying their limited light-harvesting capacity for photocarrier generation. In contrast, the absorption edge of the $ZnIn_2S_4$ catalyst was shifted to 517 nm, relevant to its inherent optical band gap of 2.40 eV, which indicates that $ZnIn_2S_4$ can be excited under visible light to produce a high density of photocarriers to contribute favorably to the PC process.[25]

After integrating ZnO and Al_2O_3 nanoparticles, the Zn−Al catalyst manifested a redshift and blueshift in the absorption threshold compared to Al_2O_3 and ZnO, respectively. This phenomenon could be explained on the basis of synergism between two materials, which consequently introduced more energy levels between ZnO and Al_2O_3 due to the formation of heterojunction. Moreover, the optical absorption character-istics of Zn−ZIS and Zn−Al−ZIS catalysts also showed a redshift contrasted to pure ZnO due to the adequate light harvesting potential of $ZnIn_2S_4$. The redshift identifies that Zn−ZIS and ZIS−Zn−Al catalysts can gather more visible light and generate additional photocarriers, promoting PC activity.[17] Notably, the Zn−ZIS and ZIS−Zn−Al catalysts revealed absorption edges at 433.3 and 465 nm with optical band gaps of 2.86 and 2.67 eV, respectively. Among all catalysts, ZIS−Zn−Al catalyst showed the strongest optical absorption due to the integration of ZnO, Al_2O_3, and $ZnIn_2S_4$, consequently boosting the production of charges for high PC activity.

3.4. Charge Separation Analysis. PL analysis is an efficient technique to detect photocarrier transfer and recombination efficiency at the surface of catalysts.[24] Generally, quenched PL emission intensity divulges the inhibited recombination of photocarriers and vice versa.[22] In Figure 3b, PL spectra of pure ZnO catalyst showed high PL intensity due to the swift recombination of photocarriers ($e^−$/h^+). The pure ZnO displayed four characteristics of PL emission bands as follows: (i) UV emission band at 390 nm due to band-to-band recombination of free excitons, (ii) violet emission band at 440 nm due to recombination of electrons localized at Zn interstitials with the VB holes, (iii) blue-green emission band at 490 nm owing to electrons transfer from shallow donor levels of Zn interstitials to an acceptor level of oxygen vacancies in ZnO, and (iv) green emission band at 510 nm due to recombination of VB holes with electrons trapped at oxygen vacancies.[25] Pure Al_2O_3 exhibited two characteristic emission peaks located at 405 and 510 nm, which are due to oxygen deficiencies in different charge states.[26] In comparison to pure ZnO, the intensity of the emission band attributed to the band gap recombination of photocarriers exhibits severe quenching for binary catalysts, implying that recombination of photocarriers is highly restrained after coupling of ZnO with Al_2O_3 and $ZnIn_2S_4$, respectively.[11] Although pure ZnO and Al_2O_3 can harvest only UV light, integrating these nanoma-terials into $ZnIn_2S_4$ could provide delayed recombination of photocarriers. The ternary ZIS−Zn−Al catalyst was identified to possess the smallest intensity of PL emission signal contrasted to binary catalysts. The main reasons for this reduced radiative recombination of photocarriers over ZIS−Zn−Al catalyst are as follows: (i) the generation of multi-charge transfer channels due to the interaction of ZnO with Al_2O_3 and ZnO to enhance the electron mobility, (ii) the electrons capturing ability of Al_2O_3 can cause some photo-electrons to diffuse on its surface to suppress the reuniting of photocarriers ($e^−$/h^+), (iii) stronger transparency of $ZnIn_2S_4$ permits effective penetration of light into ZnO and Al_2O_3, and (iv) various intrinsic vacancies of ZnO in combination with Al_2O_3 and $ZnIn_2S_4$ could support ZIS−Zn−Al to manifest wider optical response. Therefore, the synergistic effect caused the spatial separation and prolonged lifetime of photocarriers

in ZIS−Zn−Al contrasted to other catalysts. The further striking information is that the PL emission signal of Zn−ZIS and ZIS−Zn−Al catalysts exhibited an obvious red shift in the position of the UV emission band compared to that of pure ZnO, which identifies a decline in the band gap energy. In contrast, the blueshift in the UV emission signal for the Zn−Al catalyst compared to that of pure ZnO indicates an enhancement in its optical band gap, consistent with the results of DRS.[22]

3.5. FTIR Analysis. The structural information of the prepared ZnO, Zn−Al, Zn−ZIS, and ZIS−Zn−Al catalysts was examined through an FTIR study. The pure ZnO in Figure 4
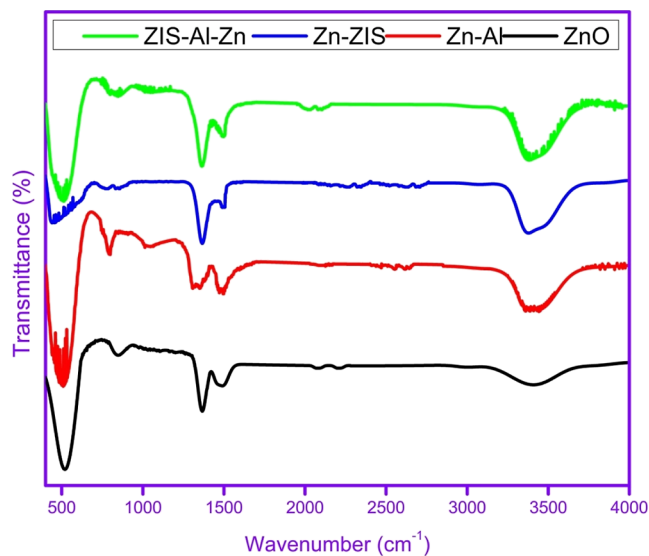
Figure 4. FTIR analysis of as-prepared ZnO, Zn−Al, Zn−ZIS, and ZIS−Zn−Al catalysts.

has a robust absorption mode at 511 cm^{-1} corresponded to Zn−O stretching vibrations for ZnO, confirming the fabrication of ZnO nanoparticles. Two absorption bands that appeared at 1370 and 1490 cm^{-1} for ZnO were attributed to C−O and O−H stretching modes, whereas an absorption peak at 3420 cm^{-1} was referred to O−H stretching modes of water adhered on the surface.[27]

Although the different absorption bands of pure ZnO were all preserved in the binary and ternary heterojunctions, there are some obvious distinctions in the intensities of stretching modes at 511 and 3420 cm^{-1}.[28] The intensity of the O−H stretching mode was observed to be maximum in ZIS−Zn−Al heterojunctions, which as a result, exhibited an enhancement in the hydrophilicity of the designed composite. That is why, the polarity of each semiconductor in the fabricated ZIS−Zn−Al heterojunction was enhanced to indicate the powerful interaction among ZnO, Al$_2$O$_3$, and ZnIn$_2$S$_4$.[29] Moreover, an increase in the intensity of the O−H stretching mode also identified the generation of more •OH radicals to boost the PC activity of the ZIS−Zn−Al composite.[30] A strong absorption band originated at 790 cm^{-1} for the Zn−Al catalyst was assigned to a stretching mode of the Zn−Al bond, whereas a wide absorption band appeared in the range 730−920 cm^{-1} confirmed the coupling of ZnIn$_2$S$_4$ with ZnO in the Zn−ZIS composite.[26] Further confirmation of heterojunctions construction was brought by the significant blue- and redshift in the position of the absorption peak that appeared at 511 cm^{-1}

for Zn−ZIS and Zn−Al catalysts contrasted to that of ZnO, respectively, which indicated that the conjugated system of ZnO somewhat deteriorated and effective interfacial interaction produced among different semiconductors in the resulting composites.[23] Therefore, FTIR results revealed that ZnO, Al$_2$O$_3$, and ZnIn$_2$S$_4$ establish an intimate interfacial contact to accelerate the transfer of photocarriers.

3.6. Textural Analysis. The textural characteristics of as-fabricated catalysts are of vital importance for the surface reaction. Therefore, the surface area is often considered a key factor in approximating the efficiency of PC reaction.[19] Generally, a large surface area is needed for high adsorption capacity for water and ensuring a maximum number of active sites for the occurrence of interfacial redox reactions to promote the PC water-splitting process.[28] The N$_2$ adsorption−desorption isotherm in Figure 5a showed that the ternary ZIS−Zn−Al catalyst exhibited a surface area of 94.77 m^2 g^{-1}, which is registered to be far superior contrasted to that of 14.65 m^2 g^{-1} for pure ZnO. The high surface area revealed the presence of abundant water adsorption sites and H$_2$ production active sites on the ZIS−Zn−Al catalyst, thereby might accelerate the rate of surface photoreactions for H$_2$ production. The large surface area might be assigned to the preparation of a ternary composite to lower the aggregation of nanoparticles and increase their dispersibility. Therefore, it is anticipated that a superior surface area of ternary composite might be handy for increasing the amount of H$_2$ production.

3.7. Photoelectrochemical Study. To check the separation and transportation trend of photocarriers at the interface of as-fabricated ZnO, Zn−Al, Zn−ZIS, and ZIS−Zn−Al catalysts, the PEC studies were conducted through EIS, CV, and LSV, and the corresponding results are illustrated in Figure 5b,c.

Generally, smaller arc diameter of EIS Nyquist plots reveals higher conductivity and prolonged separation of photocarriers and vice versa.[31] After coupling Al$_2$O$_3$ and ZnIn$_2$S$_4$ with ZnO, the arc diameter declines clearly, implying a decrease of impedance to promote the transfer of photocarriers in binary catalysts, as shown in Figure 5b. It is evident that the Zn−ZIS catalyst exhibited a lower arc radius than Zn−Al and ZnO catalysts, identifying stronger photocarrier transport behavior after integrating ZnIn$_2$S$_4$. The ZIS−Zn−Al catalyst disclosed the lowest arc diameter, confirming the intimate interfacial interaction among ZnO, Al$_2$O$_3$, and ZnIn$_2$S$_4$ semiconductors, effectively decreasing the photocarrier's transport resistance, thereby improving the separation and interfacial transport of photocarriers. To further evaluate the interfacial dynamics of photocarriers and current density, an LSV study of the prepared catalysts was conducted. All the synthesized catalysts revealed a positive anodic current, signifying the n-type semiconducting behavior of the catalysts.[32] As illustrated in Figure 5c, the pure ZnO exhibits the maximum photocurrent density of 1.15 mA/cm^2 in the anodic region, which can be assigned to its large band gap to hinder the transfer of photocarriers. With the coupling of Al$_2$O$_3$ and ZnO, the photocurrent density enhances to 1.55 mA/cm^2 due to a decrease in band gap energy to harvest more visible light. In contrast, the Zn−ZIS catalyst manifests higher anodic photocurrent density (2.42 mA/cm^2), which is approximately 2.1 times and 1.56 times superior to that of ZnO and ZnAl catalysts, implying that the construction of binary heterojunctions between ZnO and ZnIn$_2$S$_4$ increased the visible light harvesting capacity and synergistic interaction between ZnO
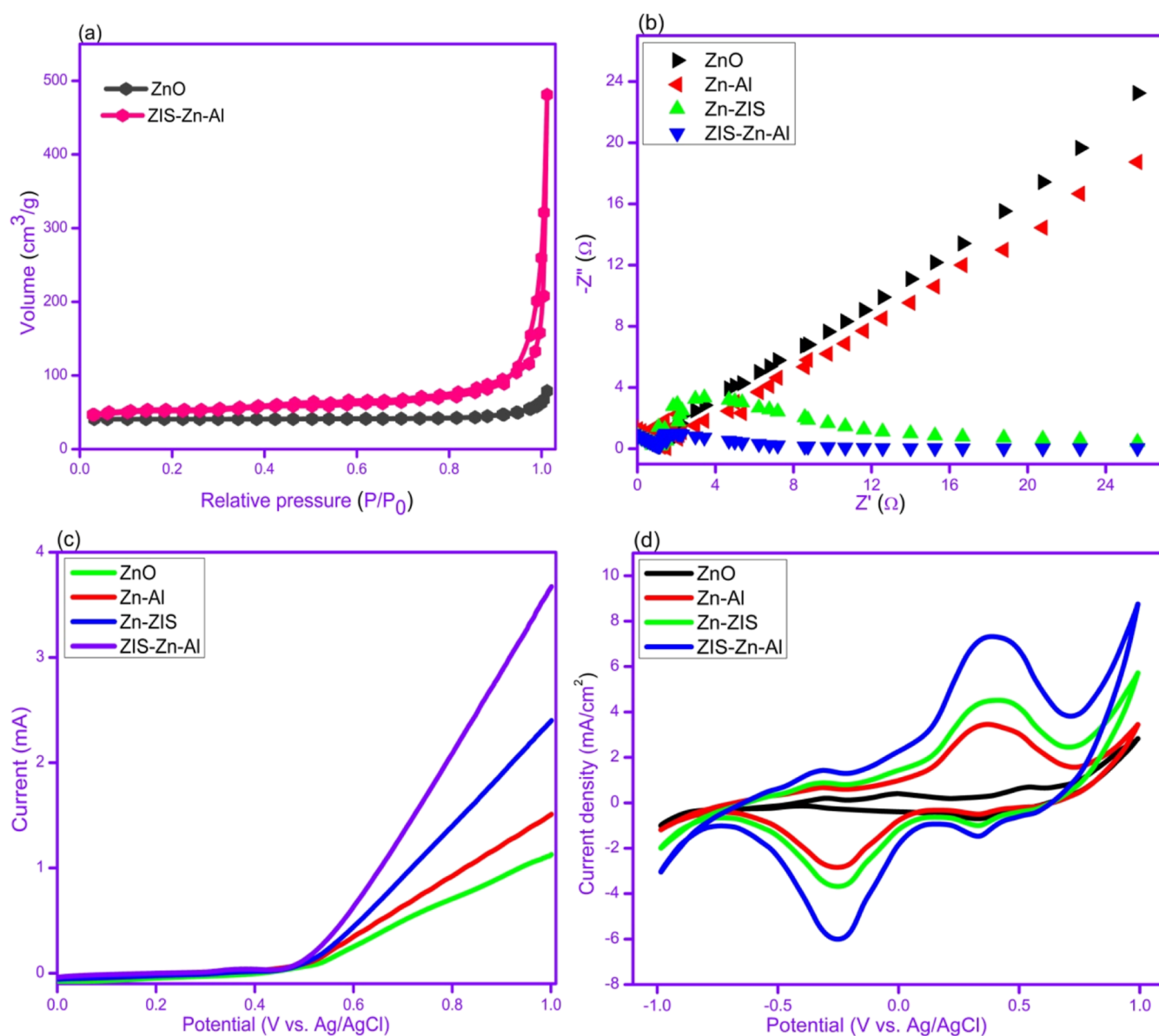
Figure 5. (a) Adsorption–desorption isotherm of ZnO and ZIS–Zn–Al catalysts, (b) EIS Nyquist plots, (c) LSV curves, and (d) *CV* curves of as-prepared ZnO, Zn–Al, Zn–ZIS, and ZIS–Zn–Al catalysts.

and $ZnIn_2S_4$ provided a large number of transport channels for charges to improve the separation and transport of photocarriers.[33] The ternary ZIS–Zn–Al catalyst showed the highest photocurrent density of 3.68 mA/cm^2, nearly 3.2 times larger than that of pure ZnO. It is believed that the coupling of ZnO, Al_2O_3, and $ZnIn_2S_4$ further triggers the electrons transfer at the interfaces due to the formation of the double built-in electric field, which consequently stimulates the separation and interfacial transport of photocarriers to reduce their recombination. In addition, the highest surface area of the ZIS–Zn–Al catalyst facilitated the high density of active sites and boosted the migration and separation efficiency of photocarriers, thereby accelerating the H_2 production rate. Therefore, LSV results indicate that smaller band bending transpired in the ZIS–Zn–Al composite for superior separation and transport of photocarriers to accelerate the PC H_2 production performance.

Figure 5d reports *CV* scans of as-prepared ZnO, Zn–Al, Zn–ZIS, and ZIS–Zn–Al catalysts obtained at a scan rate of 30 mV/s in the range of −1 to +1 V using 1 M aqueous solution of KOH as electrolyte. *CV* scan of pure ZnO manifested the smallest current response and negligible redox behavior. The current density for Zn–Al was much higher than that of pure ZnO for both forward and reverse scans, indicating a cathodic current density of 0.0348 mA/cm^2 at 0.3619 V and anodic current density of −0.0287 mA/cm^2 at −0.2419 V, implying higher catalytic ability of Zn–Al composite for H_2 production. This improvement in the redox behavior is attributed to a large surface area of Zn–Al than ZnO to provide a high density of active sites to accelerate the occurrence of redox reactions.[32,33] *CV* analysis showed that the highest anodic current density (0.0735 mA/cm^2) and cathodic current density (−0.0606 mA/cm^2) was achieved in the presence of ZIS–Zn–Al composite due to a synergistic interaction of three semiconductors which consequently generated more electrons transport channels among them to boost the migration of charge carriers by promoting the separation possibility of photocarriers and simultaneously

reduced the recombination rate of photocarriers. A large surface area produces an excessive active site generally required for efficient redox reactions.[34] Table 1 illustrates the anodic

**Table 1. Different Electrode Responses of *CV* Curves of the Prepared Catalysts**

electrode	I_{pa} (mA/cm^2)	I_{pc} (mA/cm^2)	E_{pa} (V)	E_{ca} (V)
ZnO	0.0073	−0.003	0.4512	−0.2457
Zn−Al	0.0348	−0.0287	0.3619	−0.2419
Zn−ZIS	0.0454	−0.0373	0.4090	−0.2474
ZIS−Zn−Al	0.0735	−0.0606	0.4012	−0.2523

current (I_{pa}) and cathodic current (I_{pc}) response of different catalysts. Therefore, based on EIS, LSV, and *CV* studies, it can be rationally deduced that efficient PC H$_2$ production over ZIS−Zn−Al can be credited to the remarkable separation and mobility of photocarriers among the three contributing components.

4. PC ACTIVITY

The PC H$_2$ production performance of all as-fabricated catalysts tested under visible light illumination with glycerol (10 vol %) served as a hole scavenger. The controlled experiment with the only catalyst or without a visible light source produced an insignificant quantity of H$_2$, implying the importance of photocatalysts for H$_2$ production. Figure 6a reveals that pure ZnO and Al$_2$O$_3$ cause negligible H$_2$ production, indicating that both these catalysts are inactive under visible light illumination. In contrast, despite strong visible light harvesting ability, the ZnIn$_2$S$_4$ photocatalyst produced only a small quantity of H$_2$ (0.094 mmol g$^{−1}$ h$^{−1}$), which can be attributed to the serious recombination rate of photocarriers (e$^{−}$/h^{+}).

4.1. Effect of Al$_2$O$_3$ Weight in Zn−Al Composite. To determine the optimum content of Al$_2$O$_3$ in the Zn−Al composite, ZnO was integrated with 10, 20, 30, 40, and 50 wt % of Al$_2$O$_3$ to construct various Zn−Al composites to study their PC H$_2$ production under visible light illumination. The H$_2$ production rate in Figure 6b increased with the
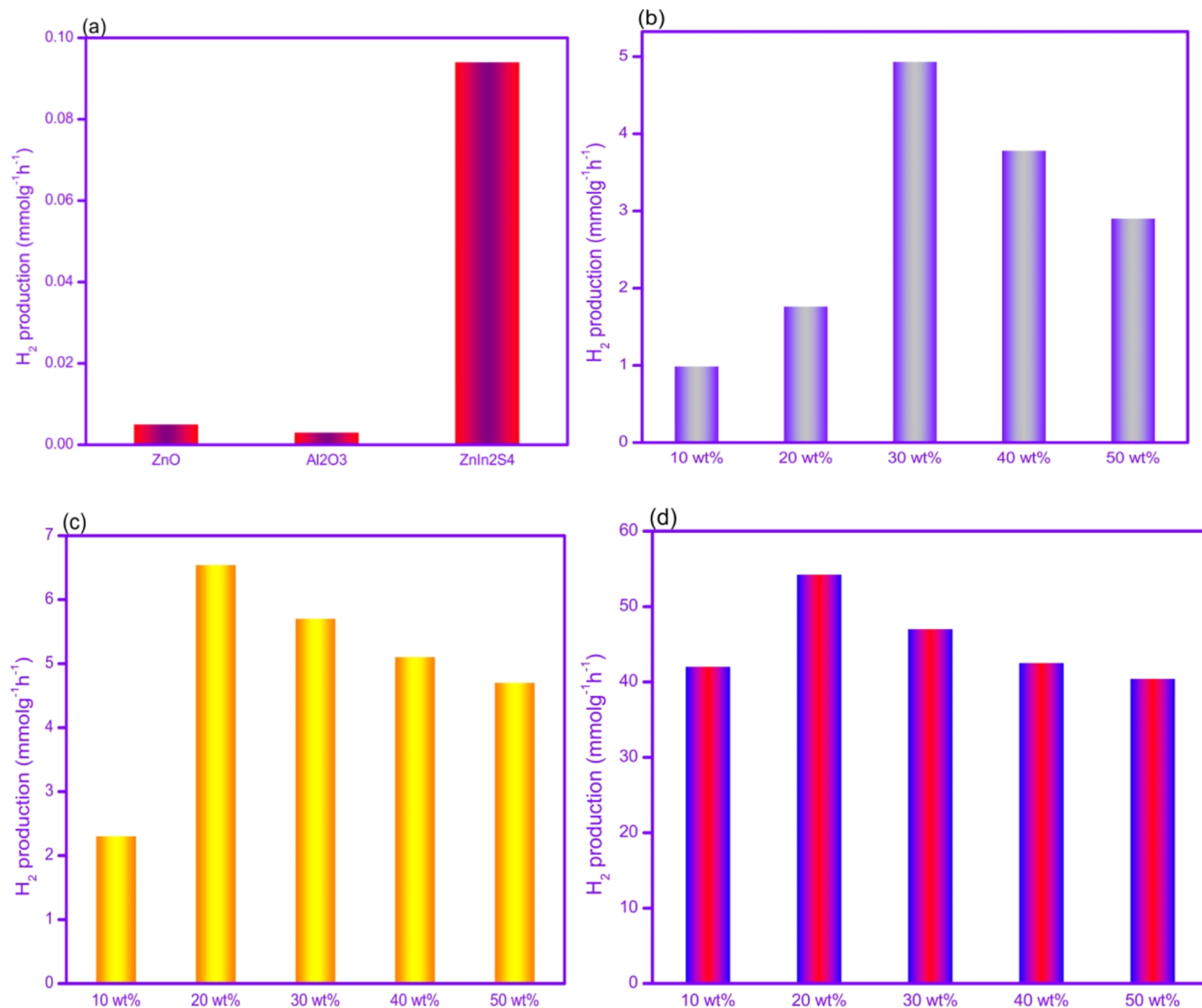
Figure 6. PC activity of (a) pure ZnO, Al$_2$O$_3$, and ZnIn$_2$S$_4$; (b) ZnO coupled with 10, 20, 30, 40, and 50 wt % of Al$_2$O$_3$; (c) ZnO coupled with 10, 20, 30, 40, and 50 wt % of ZnIn$_2$S$_4$; and (d) ZnO−Al$_2$O$_3$ coupled with 10, 20, 30, 40, and 50 wt % of ZnIn$_2$S$_4$ from the water−glycerol mixture.

concentration of Al_2O_3 to a certain limit and then showed a gradual decrease with further enhancement in the concentration of Al_2O_3, which obviously showed the influence of interfaces in heterojunction in increasing the PC activity. The maximum H_2 production rate by 30 wt % Zn−Al composite was 4.93 mmol g^{-1} h^{-1}, which was nearly 3.5 and 2.8 times greater than those of 10 wt % Zn−Al and 20 wt % Zn−Al composites and about 1.3 and 1.7 times lower contrasted to that of 40 wt % Zn−Al and 50 wt % Zn−Al composites, respectively. The highest H_2 production with Zn−Al composite at Al_2O_3 mass weight of 30% was possible due to the synergistic effect between two semiconductors, inhibited charge recombination, extended optical absorption and high mobility of charge carriers.[20] Besides, the smaller H_2 production performance of Zn−Al composite at excessive addition of Al_2O_3 would consequent from the reduced density of reduction heterogeneous sites, enhanced aggregation of particles to reduce the effective surface area, and generation of charge recombination centers to impede the separation and transfer of photocarriers.[26]

4.2. Effect of $ZnIn_2S_4$ Weight in Zn−Al Composite.

The PC H_2 production over serial Zn−ZIS catalysts was also evaluated to find the optimum content of $ZnIn_2S_4$ in the Zn−ZIS composite. In Figure 6c, the H_2 production rate of Zn−ZIS with 10 wt % $ZnIn_2S_4$ content was 4.45 mmol g^{-1} h^{-1} after 4 h of visible light illumination. After increasing the $ZnIn_2S_4$ weight to 20 wt %, the PC H_2 production activity of the Zn−ZIS composite was significantly enhanced to 6.54 mmol g^{-1} h^{-1} due to the synergistic effect of intimate contact between ZnO and $ZnIn_2S_4$, increased surface area to provide more reduction sites, the redshift in the light absorption, and abundant charge migration channels to enhance the mobility and separation of photocarriers.[22] Meanwhile, the PC H_2 production efficiency of the Zn−ZIS catalyst was further affected by adding more weight of Al_2O_3. At 30 wt % of $ZnIn_2S_4$, the lower H_2 production rate of 5.7 mmol g^{-1} h^{-1} was obtained over the Zn−ZIS catalyst, which was further reduced to 4.7 mmol g^{-1} h^{-1} when the weight of Al_2O_3 was increased to 50 wt % due to shielding of exposed active sites for H_2 production and poor light harvesting due to presence of the excess amount of $ZnIn_2S_4$ and thereby lowers the generation of photocarriers, resulting in reduced H_2 production.[29]

4.3. Optimization of ZIS−Zn−Al Composite.

The optimized binary Zn−Al composite was further coupled with various weights of $ZnIn_2S_4$ (10−50 wt %) to determine the optimal weight percentage of $ZnIn_2S_4$ in the ZIS−Zn−Al composite to demonstrate the best PC H_2 production performance. Figure 6d illustrates the effect of different weight content of $ZnIn_2S_4$ on the PC H_2 production activity of the ZIS−Zn−Al composite. When the weight percentage of $ZnIn_2S_4$ in the ZIS−Zn−Al composite was 10 and 20 wt %, the H_2 production rates reached 42 and 54.22 mmol g^{-1} h^{-1}, respectively after 4 h of light exposure. This can be attributed to the suppressed recombination of photocarriers, the high density of active sites, and enhanced visible light absorption by the synergistic interaction among ZnO, Al_2O_3, and $ZnIn_2S_4$. When the weights of the $ZnIn_2S_4$ were 30 and 40 wt %, the H_2 production of the ZIS−Zn−Al catalyst was 47 and 42.5 mmol g^{-1} h^{-1}, respectively, after 4 h of visible light illumination. This is because the high density of $ZnIn_2S_4$ particles caused aggregation and blocked the active surface of the catalyst, consequently reducing the density of heterogeneous reduction sites to exhibit quenched H_2 production performance.[28]

Although the addition of higher content of $ZnIn_2S_4$ generated abundant reducing electrons under visible light to react with H^+ to produce H_2; however, excessive content of $ZnIn_2S_4$ can act as recombination centers to increase the recombination of photocarriers.[35] Therefore, based on the H_2 production results, the weight percentage of 20 wt % is the optimal content of $ZnIn_2S_4$ in ZIS−Zn−Al composite for efficient H_2 production.

To understand the possible reason for these efficient PC results, it is mandatory to evaluate the primary scientific factors, i.e., light harvesting aptitude, the density of active sites, and the separation and transfer tendency of photocarriers. As mentioned above, the visible light response of pure $ZnIn_2S_4$ catalyst is much wider than that of ZIS−Zn−Al, which indicates that $ZnIn_2S_4$ would manifest a much better H_2 production rate than that of ZIS−Zn−Al. However, as explained earlier, pure $ZnIn_2S_4$ catalyst had shown an H_2 production rate of only 0.094 mmol g^{-1} h^{-1} in comparison to 54.22 mmol g^{-1} h^{-1} of ZIS−Zn−Al catalyst, which consequently revealed that light-harvesting range could not be the deciding factor to justify the improvement in the PC H_2 production activity of the ZIS−Zn−Al composite.

It is also obvious that the ZIS−Zn−Al composite had demonstrated the highest LSV current density, smallest EIS arc radius, and most quenched PL intensity, identifying its reasonable conductivity and high spatial separation of charge carriers due to strong interfacial interactions and abundant rapid charge transfer channels, leading to remarkable separation and migration of photocarriers. Finally, the ZIS−Zn−Al catalyst possessed the highest surface area of 94.77 m^2 g^{-1} in comparison to 14.65 m^2 g^{-1}, which certified the maximum density of active sites to speed up the occurrence of redox reactions. This above characterization results comparison suggested that active sites and swift transfer and migration of photocarriers are the primary factors for the increased PC H_2 production activity of ZIS−Zn−Al composite. The highest apparent quantum efficiency (AQE) of ZIS−Zn−Al photocatalyst was 46.4% at 420 nm. Furthermore, the ZIS−Zn−Al photocatalyst was active for H_2 evolution even at 620 nm with a modest AQE value of 6.4%.

4.4. Stability Evaluation.

Stability is quite significant for large-scale applications of the photocatalyst. The photostability of the ZIS−Zn−Al photocatalyst was evaluated for H_2 production under visible light. After each experiment, the catalyst was separated, rinsed, and dried before utilizing it for the next experiment. Figure 7 shows that the H_2 production remained almost stable, manifesting only 6% loss after five successive cycles. Therefore, the ZIS−Zn−Al photocatalyst remained highly stable, as verified by a modest loss in H_2 production. Table 2 shows the PC H_2 evolution comparison of the present work with earlier reported works.

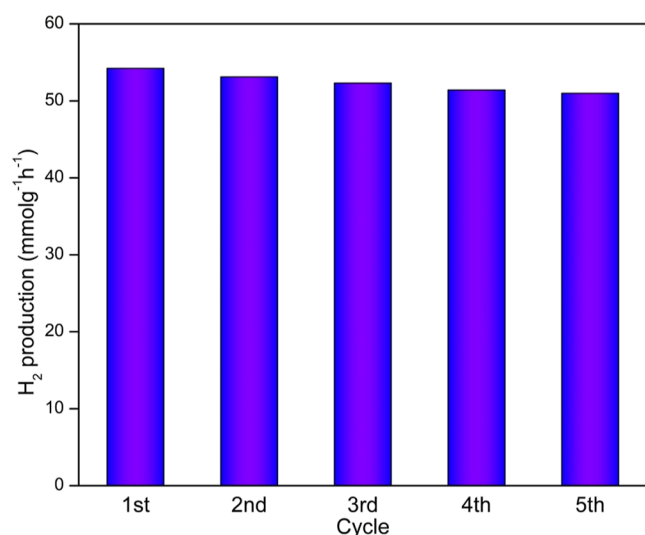### 4.5. Plausible Photocarriers Transfer Mechanism.

The CB potential (E_{CB}) and VB potential (E_{VB}) were found using the following equations[49]

$$E_{VB} = \chi - E_c + 0.5E_g \tag{1}$$

$$E_{CB} = E_{VB} - E_g \tag{2}$$

where χ, E_c, and E_g represent the electronegativity of the considered semiconductor, the energy of free electrons (4.5 eV vs NHE), and optical band gap energy, respectively. The calculated values of E_{CB} and E_{VB} are given in Table 3.

The band energy positions of ZnO, Al_2O_3, and $ZnIn_2S_4$ were determined using M−S plots.[46] The positive slopes of M−S

Figure 7. Stability test for H_2 production in the presence of the ZIS–Zn–Al catalyst.

Table 3. E_{CB} and E_{VB} Values of ZnO, Al_2O_3, and $ZnIn_2S_4$ Catalysts

catalyst	E_g (eV)	χ (eV)	E_{VB} (eV)	E_{CB} (eV)
ZnO	3.23	5.79	2.91	−0.32
Al_2O_3	3.15	5.33	2.40	−0.75
$ZnIn_2S_4$	2.40	4.86	1.55	−0.86

to identify the oxidative and reductive nature of these materials. ZnO with the highest Φ and lowest E_F values possessed the characteristics of oxidative photocatalyst, whereas the smaller values of Φ and E_F for $ZnIn_2S_4$ and Al_2O_3 relative to ZnO deemed them as reductive photocatalysts.[50] Therefore, when ZnO, Al_2O_3, and $ZnIn_2S_4$ are coupled, the electrons on $ZnIn_2S_4$ and Al_2O_3 would spontaneously flow to ZnO until their E_F levels reach an equilibrium. As a consequence of this charge flow process, upward band bending occurred for $ZnIn_2S_4$ and Al_2O_3 due to the lowering of their electron densities. On the contrary, ZnO with increased electron density manifested downward band bending.[51] Meanwhile, the buildup of positively and negatively charged layers originated on both sides of the interface, creating potential differences and producing an internal electric field (IEF) at the interface.[52] The IEF and band bending are the characteristic features of the S-scheme. The synergistic effect of EIF and band bending effectively promotes the transfer of photocarriers to follow the S-scheme mechanism. Based on work functions, DRS results, and M–S plots, a possible photocarrier transfer mechanism over the ZIS–Zn–Al composite can be either type II or S-scheme. If the prepared ternary ZIS–Zn–Al heterojunctions pursue a traditional photocarriers (e^-/h^+) transfer route, and then, depending on the band edges potential, the photoelectrons transfer from the CB of $ZnIn_2S_4 \rightarrow Al_2O_3 \rightarrow ZnO$ through the interfaces, whereas holes flow in the reverse direction from the VB of $ZnO \rightarrow Al_2O_3 \rightarrow ZnIn_2S_4$. Although the recombination rate of photocarriers can be effectively restrained, the accumulated photoelectrons at the CB of ZnO and holes at the VB of $ZnIn_2S_4$ lose their strong reducibility and oxidizability, respectively. Furthermore, the E_{CB} value of ZnO (−0.33 V vs NHE) is less negative than the standard redox potential of H^+/H_2 (−0.41 V vs NHE). Therefore, photoelectrons at the CB of ZnO could not reduce H^+ to H_2. Consequently, it is proposed that the conventional photocarrier transfer mechanism in type II heterojunction unavoidably possesses some limitations in the ZIS–Al–Zn system.

plots, as illustrated in Figure 8a–c indicate that ZnO, Al_2O_3, and $ZnIn_2S_4$ are negative semiconductors and corresponding flat band potentials (E_{FB}) at the Ag/AgCl scale were measured to be −0.43, −0.89, and −0.96 V, respectively. Using the conversion formula $E_{NHE} = E_{Ag/AgCl} + E^0_{Ag/AgCl}$), these potentials were then converted into −0.23, −0.69, and −0.76 V versus NHE for ZnO, Al_2O_3, and $ZnIn_2S_4$, respectively, where $E^0_{Ag/AgCl}$ = 0.197 at pH = 7.[41] Usually, the E_{FB} in an n-type semiconductor is 0.1 V more positive than E_{CB}.[47] Therefore, E_{CB} values of ZnO, Al_2O_3, and $ZnIn_2S_4$ were approximately measured as −0.33, −0.79, and −0.86 eV, respectively, and agreed with E_{CB} values measured using DRS results.

The work function is an efficient means to deduce the Fermi level (E_F), which provides information about the directional flow of electrons.[48] The work functions (Φ) of ZnO, Al_2O_3, and $ZnIn_2S_4$ semiconductors were calculated using the E_F values versus NHE and converting them relative to the vacuum level via the equation: $E_{F(vs\ vac)} = -4.5 - E_{F(vs\ NHE)}$.[49] The obtained values of Φ for ZnO, Al_2O_3, and $ZnIn_2S_4$ were −4.27, −3.82, and −3.74 eV versus NHE, respectively.[35] The Φ for ZnO, Al_2O_3, and $ZnIn_2S_4$ were found to be 4.27, 3.82, and 3.74 eV versus E_{vac}, respectively. Hence, E_F levels of these three semiconductors were in the order $ZnIn_2S_4 > Al_2O_3 > ZnO$. The results of work function (Φ) and Fermi level (E_F) can be used

Table 2. Performance Summary of the Tested PC H_2 Evolution Systems Compared to the Published Work

| photocatalyst	synthetic method	light source	H_2 evolution	sacrificial agent	refs.
$CdS/Ti^{3+}/N$-TiO_2	in situ hydrothermal	300 W Xe lamp λ > 420 nm	1118.5 μmol	Na_2S, Na_2SO_3	Qin et al.[36]
N-MoS_2/S-g-C_3N_4	thermal polycondensation	300 W Xe lamp	658.5 $\mu mol/g/h$	TEOA	Chen et al.[37]
Rh–Cu/TiO_2	deposition-precipitation with urea	UV Hg lamp λ = 254, 365, 450 nm	9260 $\mu mol/g/h$	methanol, ethanol, propanol	Camposeco et al.[38]
$CdS/NC@Mo_2N$	solvothermal	Xe lamp, 3.5 mW cm^{-2}, λ > 400 nm	7294 $\mu mol/g/h$	Na_2S, Na_2SO_3	Mu et al.[39]
MMT/g-$C_3N_4/NiCoP$	hydrothermal	300 W Xe lamp λ > 420 nm	12.5 mmol g^{-1} h^{-1}	TEOA	Xu et al.[40]
ZnS	hydrothermal	300 W Xe lamp λ > 420 nm	337.71 ± 3.72	Na_2S, Na_2SO_3	Hao et al.[41]
$MoS_2/CoAl$ LDH	hydrothermal	300 W Xe lamp	17.1 $\mu mol/g/h$	methanol	Tao et al.[42]
CdS–NiV LDH	hydrothermal	5 W LED	478.96 μmol	Na_2S, Na_2SO_3	Yang et al.[43]
Cu-$MoFs$-$Mn_{0.5}Cd_{0.95}$	hydrothermal	5 W LED λ > 420 nm	547.5 μmol	Na_2S, Na_2SO_3	Cao et al.[44]
$NiSe_2/Cd_{0.5}Zn_{0.5}S$	hydrothermal	300 W Xe lamp λ > 420 nm	121.01 mmol/g/h	Na_2S, Na_2SO_3	Zhang et al.[45]
$ZnIn_2S_4$–ZnO–Al_2O_3	combustion	300 W Xe lamp λ > 400 nm	54.2 mmol g^{-1} h^{-1}	glycerol	current study
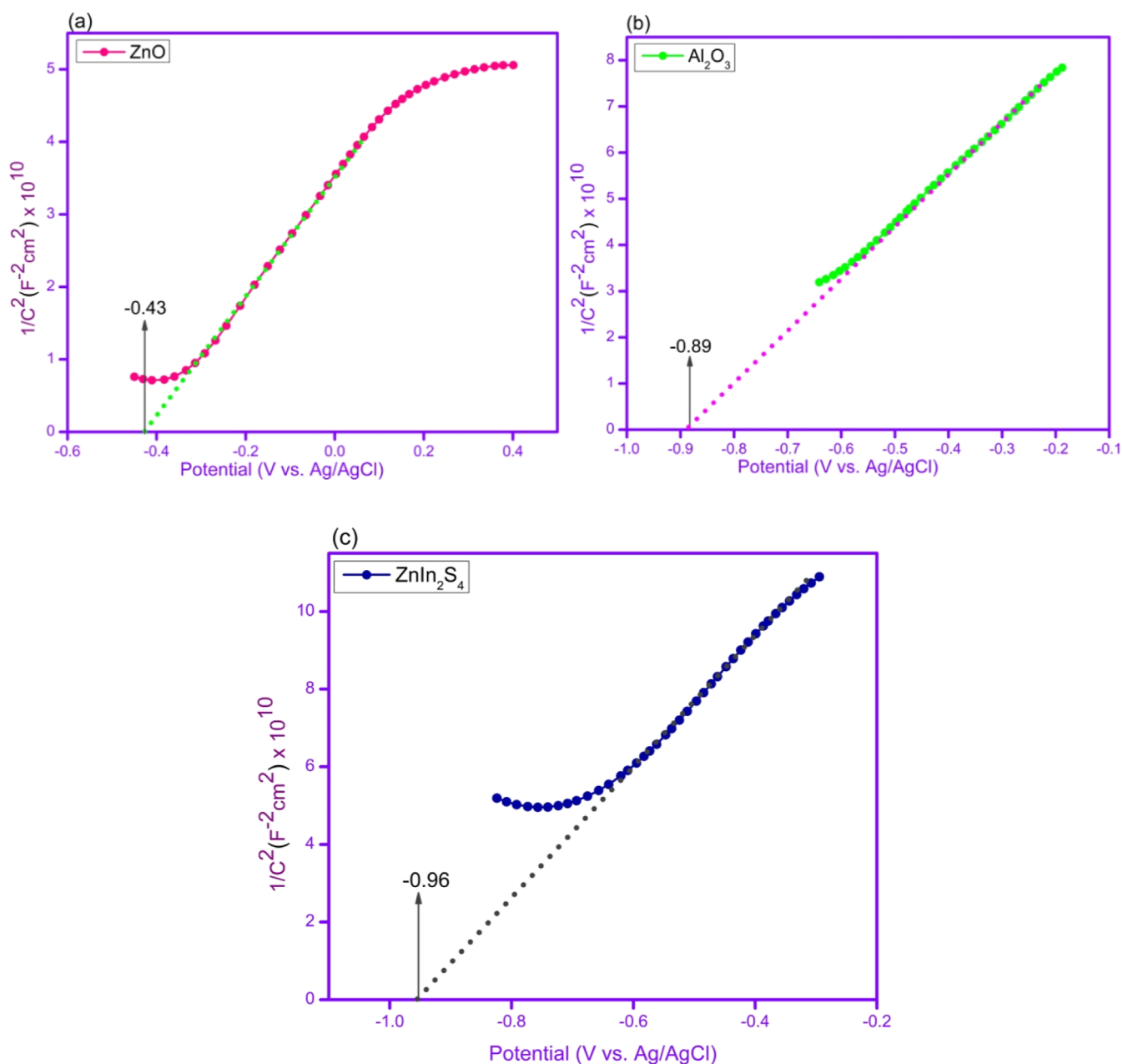
Figure 8. Mott−Schottky plots of (a) ZnO, (b) Al$_2$O$_3$, and (c) ZnIn$_2$S$_4$.

Hence, based on the mode of band edge positions, the ZIS−Al−Zn composite identifies the characteristic features of a dual S-scheme heterojunction system. During the PC H$_2$ production process, H$_2$ is produced by H$^+$ reacting with the photoelectron, and therefore, the CB of the catalyst should be more negative contrasted to H$_2$ reduction potential (−0.41 V vs NHE). Based on the above results, the CB positions of ZnIn$_2$S$_4$ and Al$_2$O$_3$ are positioned at −0.86 eV versus NHE and −0.79 eV versus NHE, while that of ZnO is located at −0.33 eV vs NHE, respectively. Therefore, the CB potential of both ZnIn$_2$S$_4$ and Al$_2$O$_3$ acquired the conditions of H$_2$ production. Under visible light, the photoelectrons at ZnO with relatively weaker reduction ability are prone to transport and perish with photo-holes at ZnIn$_2$S$_4$ and Al$_2$O$_3$ with less oxidation ability owing to the driving force delivered by an IEF, as shown in Figure 9. Accordingly, the photoelectrons with strong reducibility survived at the CB of ZnIn$_2$S$_4$ and Al$_2$O$_3$. The

holes with strong oxidation potential remained in the VB of ZnO, implying a strong separation of photocarriers and retaining their strong redox potentials to accelerate the PC H$_2$ production. The photoelectrons reserved at the CB of ZnIn$_2$S$_4$ and Al$_2$O$_3$ contained enough potential to reduce H$^+$ to produce H$_2$(H$^+$/H$_2$ = −0.41 eV vs NHE), while holes in the VB of ZnO were scavenged by sacrificial reagent TEOA.[53] Hence, following dual S-scheme heterojunctions, the recombination efficiency of photocarriers was strongly quenched, which ultimately provided a high density of photocarriers with powerful redox potentials to contribute to H$_2$ production.

5. CONCLUSIONS

In summary, the ternary ZIS−Al−Zn heterojunction was fabricated by a simple, inexpensive, and rapid combustion method and experimented with for PC H$_2$ production under visible light illumination. Contrasted to single ZnO and binary
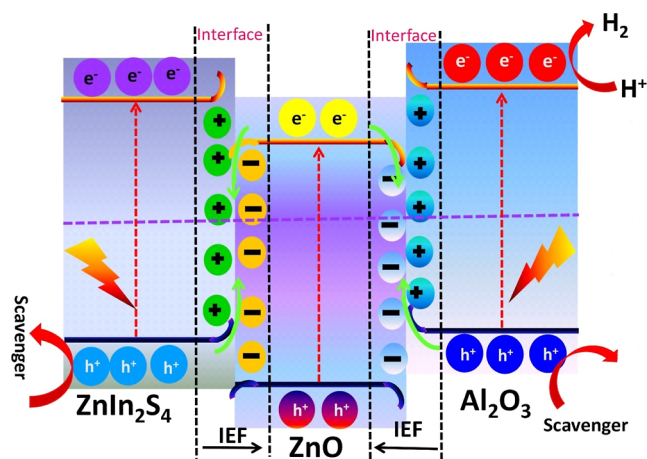
Figure 9. Possible mechanism for H_2 evolution over the $ZnIn_2S_4-ZnO-Al_2O_3$ heterojunction system under visible light illumination.

Zn−Al and Zn−ZIS photocatalysts, the ZIS−Al−Zn manifested strong separation efficiency and highly suppressed the recombination rate of photocarriers. Meanwhile, the dual S-scheme ZIS−Al−Zn heterojunctions also exhibited long-term stability and redshift in the light-harvesting due to synergistic effects among ZnO, Al_2O_3, and $ZnIn_2S_4$. The highest H_2 production rate of 54.22 mmol g^{-1} h^{-1} was achieved using 20 wt % as the optimized content of each $ZnIn_2S_4$ under visible light illumination. Moreover, the optimized ZIS−Al−Zn composite photocatalyst demonstrated efficient stability after five successive cycles for H_2 production. The present work introduces the synthesis of dual S-scheme heterojunctions by integrating ZnO with Al_2O_3 and $ZnIn_2S_4$ as an efficient photocatalyst. Still, there is high space to explore ternary heterojunctions using facile combustion techniques to not only promote the efficiency of H_2 production but also for environmental remediation.

■ AUTHOR INFORMATION

Corresponding Author

Shazia Shukrullah − *Department of Physics, University of Agriculture Faisalabad, 38040 Faisalabad, Pakistan;* orcid.org/0000-0002-4474-3768; Email: zshukrullah@gmail.com

Authors

Irshad Ahmad − *Department of Physics, University of Agriculture Faisalabad, 38040 Faisalabad, Pakistan*

Humaira Hussain − *Department of Chemistry, University of Okara, 56300 Okara, Pakistan*

Muhammad Yasin Naz − *Department of Physics, University of Agriculture Faisalabad, 38040 Faisalabad, Pakistan;* orcid.org/0000-0002-8490-7819

Muhammad Irfan − *Electrical Engineering Department, College of Engineering, Najran University, 61441 Najran, Saudi Arabia;* orcid.org/0000-0003-4161-6875

Othman Alyahyawy − *King Abduaziz Hospital, King Abdualziz University, 21589 Jeddah, Saudi Arabia*

Morooj A. Al thagafi − *College of Science, Department of Modesty, Jeddah University, 23218 Jeddah, Saudi Arabia*

Complete contact information is available at:
https://pubs.acs.org/10.1021/acsomega.3c02267

■ REFERENCES

(1) Alsulami, Q. A.; Rajeh, A.; Mannaa, M. A.; Albukhari, S. M.; Baamer, D. F. Preparation of highly efficient sunlight driven photodegradation of some organic pollutants and H_2 evolution over rGO/FeVO4 nanocomposites. *Int. J. Hydrogen Energy* 2021, *46*, 27349−27363.

(2) Fu, Z.; Ma, X.; Xia, B.; Hu, X.; Fan, J.; Liu, E. Efficient photocatalytic H_2 evolution over Cu and Cu3P co-modified TiO2 nanosheet. *Int. J. Hydrogen Energy* 2021, *46*, 19373−19384.

(3) Bahadoran, A.; Masudy-Panah, S.; De Lile, J. R.; Li, J.; Gu, J.; Sadeghi, B.; Ramakrishna, S.; Liu, Q. Novel 0D/1D ZnBi2O4/ZnO S-scheme photocatalyst for hydrogen production and BPA removal. *Int. J. Hydrogen Energy* 2021, *46*, 24094−24106.

(4) Liang, S.; Sui, G.; Li, J.; Guo, D.; Luo, Z.; Xu, R.; Yao, H.; Wang, C.; Chen, S. ZIF-L-derived porous C-doped ZnO/CdS graded nanorods with Z-scheme heterojunctions for enhanced photocatalytic hydrogen evolution. *Int. J. Hydrogen Energy* 2022, *47*, 11190−11202.

(5) Ramírez-Ortega, D.; Guerrero-Araque, D.; Acevedo-Peña, P.; Reguera, E.; Calderon, H. A.; Zanella, R. Enhancing the photocatalytic hydrogen production of the ZnO−TiO2 heterojunction by supporting nanoscale Au islands. *Int. J. Hydrogen Energy* 2021, *46*, 34333−34343.

(6) Mohammadi, I.; Zeraatpisheh, F.; Ashiri, E.; Abdi, K. Solvothermal synthesis of g-C3N4 and ZnO nanoparticles on TiO2 nanotube as photoanode in DSSC. *Int. J. Hydrogen Energy* 2020, *45*, 18831−18839.

(7) Guo, X.; Liu, X.; Yan, J.; Liu, S. F. Heteroepitaxial growth of core-shell ZnO/CdS heterostructure for efficient and stable photo-catalytic hydrogen generation. *Int. J. Hydrogen Energy* 2022, *47*, 34410−34420.

(8) Mugunthan, E.; Saidutta, M. B.; Jagadeeshbabu, P. E. Photocatalytic activity of ZnO-WO3 for diclofenac degradation under visible light irradiation. *J. Photochem. Photobiol., A* 2019, *383*, 111993.

(9) Bagtache, R.; Saib, F.; Abdmeziem, K.; Trari, M. A new hetero-junction p-CuO/Al2O3 for the H_2 evolution under visible light. *Int. J. Hydrogen Energy* 2019, *44*, 22419−22424.

(10) Goudarzi, M.; Salavati-Niasari, M. Using pomegranate peel powders as a new capping agent for synthesis of CuO/ZnO/Al2O3 nanostructures; enhancement of visible light photocatalytic activity. *Int. J. Hydrogen Energy* 2018, *43*, 14406−14416.

(11) Janani, B.; Syed, A.; Raju, L. L.; Bahkali, A. H.; Al-Rashed, S.; Elgorban, A. M.; Ahmed, B.; Thomas, A. M.; Khan, S. S. Designing intimate porous Al2O3 decorated 2D CdO nano-heterojunction as enhanced white light driven photocatalyst and antibacterial agent. *J. Alloys Compd.* 2022, *896*, 162807.

(12) Janani, B.; Syed, A.; Hari Kumar, B.; Elgorban, A. M.; Bahkali, A. H.; Ahmed, B.; Das, A.; Sudheer Khan, S. High performance MnO2−Al2O3 nanocomposite as white light photocatalyst and bactericidal agent: insights on photoluminescence and intrinsic mechanism. *Opt. Mater.* 2021, *120*, 111438.

(13) Magnone, E.; Kim, M. K.; Lee, H. J.; Park, J. H. Facile synthesis of TiO2-supported Al2O3 ceramic hollow fiber substrates with extremely high photocatalytic activity and reusability. *Ceram. Int.* 2021, *47*, 7764−7775.

(14) Ibrahim, S. A.; Ekinci, E. K.; Karaman, B. P.; Oktar, N. Coke-resistance enhancement of mesoporous γ-Al2O3 and MgO-supported Ni-based catalysts for sustainable hydrogen generation via steam

reforming of acetic acid. *Int. J. Hydrogen Energy* **2021**, *46*, 38281–38298.

(15) Al Farraj, D. A.; Al-Mohaimeed, A. M.; Alkufeidy, R. M.; Alkubaisi, N. A. Facile synthesis and characterization of CeO_2-Al_2O_3 nano-heterostructure for enhanced visible-light photocatalysis and bactericidal applications. *Colloid Interface Sci. Commun.* **2021**, *41*, 100375.

(16) Tahir, M. B.; Asiri, A. M.; Nawaz, T. A perspective on the fabrication of heterogeneous photocatalysts for enhanced hydrogen production. *Int. J. Hydrogen Energy* **2020**, *45*, 24544–24557.

(17) Pan, J.; Liang, J.; Xu, Z.; Yao, X.; Qiu, J.; Chen, H.; Qin, L.; Chen, D.; Huang, Y. Rationally designed ternary $CdSe/WS_2/g$-C_3N_4 hybrid photocatalysts with significantly enhanced hydrogen evolution activity and mechanism insight. *Int. J. Hydrogen Energy* **2021**, *46*, 30344–30354.

(18) Ma, D.; Shi, J. W.; Zou, Y.; Fan, Z.; Shi, J.; Cheng, L.; Sun, D.; Wang, Z.; Niu, C. Multiple carrier-transfer pathways in a flower-like $In_2S_3/CdIn_2S_4/In_2O_3$ ternary heterostructure for enhanced photo-catalytic hydrogen production. *Nanoscale* **2018**, *10*, 7860–7870.

(19) Liu, S. J.; Li, F. T.; Li, Y. L.; Hao, Y. J.; Wang, X. J.; Li, B.; Liu, R. H. Fabrication of ternary g-$C_3N_4/Al_2O_3/ZnO$ heterojunctions based on cascade electron transfer toward molecular oxygen activation. *Appl. Catal., B* **2017**, *212*, 115–128.

(20) Li, D.; Yang, C.; Rajendran, S.; Qin, J.; Zhang, X. Nanoflower-like $Ti_3CN@ TiO_2/CdS$ heterojunction photocatalyst for efficient photocatalytic water splitting. *Int. J. Hydrogen Energy* **2022**, *47*, 19580–19589.

(21) Ahmad, I.; Ahmed, E.; Ahmad, M.; Akhtar, M. S.; Basharat, M. A.; Khan, W. Q.; Ghauri, M. I.; Ali, A.; Manzoor, M. F. The investigation of hydrogen evolution using Ca doped ZnO catalysts under visible light illumination. *Mater. Sci. Semicond. Process.* **2020**, *105*, 104748.

(22) Pal, D. B.; Rathoure, A. K.; Singh, A. Investigation of surface interaction in rGO-CdS photocatalyst for hydrogen production: an insight from XPS studies. *Int. J. Hydrogen Energy* **2021**, *46*, 26757–26769.

(23) Belabed, C.; Tab, A.; Bellal, B.; Belhamdi, B.; Benrakaa, N.; Trari, M. High photocatalytic performance for hydrogen production under visible light on the hetero-junction Pani-ZnO nanoparticles. *Int. J. Hydrogen Energy* **2021**, *46*, 17106–17115.

(24) Liao, M.; Guo, C.; Guo, W.; Hu, T.; Xie, J.; Gao, P.; Xiao, H. One-step growth of $CuO/ZnO/CeO_2/ZrO_2$ nanoflowers catalyst by hydrothermal method on Al_2O_3 support for methanol steam reforming in a microreactor. *Int. J. Hydrogen Energy* **2021**, *46*, 9280–9291.

(25) Ahmad, I.; Shukrullah, S.; Hussain, H.; Naz, M. Y.; Alsaif, F. K.; Alsulamy, S.; Khan, Y. Robust S-scheme ZnO-TiO2-Ag with efficient charge separations for highly active hydrogen evolution performance and photocatalytic mechanism insight. *Appl. Catal., A* **2023**, *662*, 119259.

(26) Sun, M.; Zhou, Y.; Yu, T.; Wang, J. Synthesis of g-C_3N_4/WO_3-carbon microsphere composites for photocatalytic hydrogen produc-tion. *Int. J. Hydrogen Energy* **2022**, *47*, 10261–10276.

(27) Dang, Y.; Feng, L.; Hu, W.; Wang, W.; Zhang, Q.; Ma, B. A 3D flower-like WC with large capacitance as efficient co-catalyst in photocatalytic H_2 evolution. *Int. J. Hydrogen Energy* **2021**, *46*, 39251–39261.

(28) Yang, X.; Sun, S.; Shi, Z.; Yun, D.; Guo, Y.; Liu, C.; Yang, B.; Yang, M.; Yang, Q.; Cui, J. One-pot construction of highly efficient $TaON/Bi_2O_3/S$−BiOCl ternary photocatalysts: Simultaneously in-tegrating type- with Z-scheme junctions for improved visible light-driven removal of organic pollutants. *Chemosphere* **2022**, *307*, 135979.

(29) Valian, M.; Soofivand, F.; Yusupov, M. M.; Salavati-Niasari, M. Facile synthesis of $SrTiO_3/CoAlMnO_4$ nanocomposite: A recharge-able heterojunction photocatalyst with superior hydrogen storage capability. *Int. J. Hydrogen Energy* **2022**, *47*, 31624–31637.

(30) Noor, S.; Haider, R. S.; Noor, S.; Sajjad, S.; Khan Leghari, S. A.; Mehboob, M.; Long, M. Role of conductive channels via CQDs on

NiO/g-C_3N_4 Z-scheme composite as a bi-functional photocatalyst. *Int. J. Hydrogen Energy* **2022**, *47*, 36517–36529.

(31) Dong, H.; Xiao, M.; Zhu, D.; Zuo, Y.; Cheng, S.; Han, Z.; Li, C. $CoCO_3$ hierarchical structure embedded on g-C_3N_4 nanosheets to assemble 3D/2D Z-scheme heterojunction towards efficiently and stably photocatalytic hydrogen production. *Int. J. Hydrogen Energy* **2021**, *46*, 32044–32054.

(32) Sk, S.; Vennapoosa, C. S.; Tiwari, A.; Abraham, B. M.; Ahmadipour, M.; Pal, U. Polyaniline encapsulated Ti-MOF/CoS for efficient photocatalytic hydrogen evolution. *Int. J. Hydrogen Energy* **2022**, *47*, 33955–33965.

(33) Beshkar, F.; Al-Nayili, A.; Amiri, O.; Salavati-Niasari, M.; Mousavi-Kamazani, M. Fabrication of S-scheme $ZnO/Zn_3(PO4)_2$ heterojunction photocatalyst toward photodegradation of tetracycline antibiotic and photocatalytic mechanism insight. *Int. J. Hydrogen Energy* **2022**, *47*, 928–939.

(34) Dong, M.; Li, W.; Ren, C.; Ma, X.; Li, X.; Liu, S.; Li, Y.; Chen, S. Fabrication of novel ZnTe-based photocatalyst: Synergistic effect of dye sensitization and bridge engineering for boosting hydrogen evolution over ZnTe. *Int. J. Hydrogen Energy* **2022**, *47*, 11500–11510.

(35) Das, K. K.; Paramanik, L.; Parida, K. An insight to band-bending mechanism of polypyrrole sensitized B-$rGO/ZnFe_2O_4$pn heterostructure with dynamic charge transfer for photocatalytic applications. *Int. J. Hydrogen Energy* **2021**, *46*, 24484–24500.

(36) Qin, Y.; Li, H.; Lu, J.; Meng, F.; Ma, C.; Yan, Y.; Meng, M. Nitrogen-doped hydrogenated TiO_2 modified with CdS nanorods with enhanced optical absorption, charge separation and photo-catalytic hydrogen evolution. *Chem. Eng. J.* **2020**, *384*, 123275.

(37) Chen, Y.; Su, F.; Xie, H.; Wang, R.; Ding, C.; Huang, J.; Xu, Y.; Ye, L. One-step construction of S-scheme heterojunctions of N-doped MoS_2 and S-doped g-C_3N_4 for enhanced photocatalytic hydrogen evolution. *Chem. Eng. J.* **2021**, *404*, 126498.

(38) Camposeco, R.; Hinojosa-Reyes, M.; Zanella, R. Highly efficient photocatalytic hydrogen evolution by using Rh as co-catalyst in the Cu/TiO_2 system. *Int. J. Hydrogen Energy* **2021**, *46*, 26074–26086.

(39) Mu, R.; Ao, Y.; Wu, T.; Wang, C.; Wang, P. Synergistic effect of molybdenum nitride nanoparticles and nitrogen-doped carbon on enhanced photocatalytic hydrogen evolution performance of CdS nanorods. *J. Alloys Compd.* **2020**, *812*, 151990.

(40) Xu, J.; Qi, Y.; Wang, W.; Wang, L. Montmorillonite-hybridized g-C_3N_4 composite modified by NiCoP cocatalyst for efficient visible-light-driven photocatalytic hydrogen evolution by dye-sensitization. *Int. J. Hydrogen Energy* **2019**, *44*, 4114–4122.

(41) Hao, X.; Wang, Y.; Zhou, J.; Cui, Z.; Wang, Y.; Zou, Z. Zinc vacancy-promoted photocatalytic activity and photostability of ZnS for efficient visible-light-driven hydrogen evolution. *Appl. Catal., B* **2018**, *221*, 302–311.

(42) Tao, J.; Yu, X.; Liu, Q.; Liu, G.; Tang, H. Internal electric field induced S−scheme heterojunction $MoS_2/CoAl$ LDH for enhanced photocatalytic hydrogen evolution. *J. Colloid Interface Sci.* **2021**, *585*, 470–479.

(43) Yang, M.; Wang, K.; Li, Y.; Yang, K.; Jin, Z. Pristine hexagonal CdS assembled with NiV LDH nanosheet formed pn heterojunction for efficient photocatalytic hydrogen evolution. *Appl. Surf. Sci.* **2021**, *548*, 149212.

(44) Cao, Y.; Wang, G.; Liu, H.; Li, Y.; Jin, Z.; Ma, Q. Regular octahedron Cu-MOFs modifies $Mn_{0.05}Cd_{0.95}S$ nanoparticles to form a S-scheme heterojunction for photocatalytic hydrogen evolution. *Int. J. Hydrogen Energy* **2021**, *46*, 7230–7240.

(45) Zhang, X.; Cheng, Z.; Deng, P.; Zhang, L.; Hou, Y. $NiSe_2/Cd_{0.5}Zn_{0.5}S$ as a type-II heterojunction photocatalyst for enhanced photocatalytic hydrogen evolution. *Int. J. Hydrogen Energy* **2021**, *46*, 15389–15397.

(46) He, J. Y.; Zhang, D.; Wang, X. J.; Zhao, J.; Li, Y. P.; Liu, Y.; Li, F. T. Phosphorylation of NiAl-layered double hydroxide nanosheets as a novel cocatalyst for photocatalytic hydrogen evolution. *Int. J. Hydrogen Energy* **2021**, *46*, 18977–18987.

(47) Li, Z.; Ma, T.; Zhang, X.; Wang, Z. In_2Se_3/CdS nanocomposites as high efficiency photocatalysts for hydrogen production under visible light irradiation. *Int. J. Hydrogen Energy* **2021**, *46*, 15539−15549.

(48) Wang, K.; Li, S.; Li, Y.; Li, Y.; Wang, G.; Jin, Z. CoAl LDH in-situ derived CoAlP coupling with Ni_2P form S-scheme heterojunction for efficient hydrogen evolution. *Int. J. Hydrogen Energy* **2022**, *47*, 23618−23631.

(49) Dai, X.; Feng, S.; Wu, W.; Zhou, Y.; Ye, Z.; Cao, X.; Wang, Y.; Yang, C. Photocatalytic hydrogen evolution and antibiotic degradation by S-scheme $ZnCo_2S_4$/TiO_2. *Int. J. Hydrogen Energy* **2022**, *47*, 25104−25116.

(50) Zhang, L.; Zhang, J.; Yu, H.; Yu, J. Emerging S-scheme photocatalyst. *Adv. Mater.* **2022**, *34*, 2107668.

(51) Zhang, J.; Zhang, L.; Wang, W.; Yu, J. In situ irradiated X-ray photoelectron spectroscopy investigation on electron transfer mechanism in S-scheme photocatalyst. *J. Phys. Chem. Lett.* **2022**, *13*, 8462−8469.

(52) Ni, N.; Qie, B.; Du, S.; Sang, Z.; Wang, Q.; Meng, C.; Tong, Y. A novel all-solid-state S-scheme in CdS/ZnTHPP binary nanosystem for hydrogen evolution. *Int. J. Hydrogen Energy* **2022**, *47*, 13044−13053.

(53) Zhao, Y.; Guo, Y.; Li, J.; Li, P. Efficient hydrogen evolution with ZnO/$SrTiO_3$ S-scheme heterojunction photocatalyst sensitized by Eosin Y. *Int. J. Hydrogen Energy* **2021**, *46*, 18922−18935.